Journal of Materials Science & Technology 154 (2023) 210–216

Contents lists available at ScienceDirect

Journal of Materials Science & Technology

journal homepage: www.elsevier.com/locate/jmst

Research Article

Observation of low thermal expansion behavior and weak thermal anisotropy in M_3A_2C phases

Hongxiang Chen[a,c,d,*], Zhilong Zhang[a], Jun Deng[b], Zhijie Lin[a,c], Chunfu Hong[a,c], Shixuan Du[b,e,f], Pinqiang Dai[a,c,*]

[a] School of Materials Science and Engineering, Fujian University of Technology, Fuzhou 350118, China
[b] Institute of Physics & University of Chinese Academy of Sciences, Chinese Academy of Sciences, Beijing 100190, China
[c] Fujian Provincial Key Laboratory of Advanced Materials Processing and Application, Fuzhou 350118, China
[d] Center for Advanced Energy and Functional Materials, Fujian University of Technology, Fuzhou 350118, China
[e] Songshan Lake Materials Laboratory, Dongguan 523808, China
[f] CAS Key Laboratory of Vacuum Physics, Beijing 100049, China

ARTICLE INFO

Article history:
Received 16 November 2022
Revised 21 December 2022
Accepted 9 January 2023
Available online 11 March 2023

Keywords:
Max phase
Layered ceramics
Thermal expansion
Anisotropy
X-ray diffraction

ABSTRACT

M_3A_2X phases, named 321 phases, are an atypical series of MAX phases featuring in the MA-triangular-prism bilayers, with the A = As/P, exhibiting excellent elastic properties. This work systematically studies the thermal expansion properties of 321 phases. We found their average linear thermal expansion coefficients (TECs), α_L = 5-6 μK^{-1}, are the lowest among the reported values of MAX phases. The lowest average TEC was found in Nb_3As_2C (α_a = 4.46(4) μK^{-1}, α_c = 5.09(4) μK^{-1}, α_L = 5.09(4) μK^{-1}). The average TEC and anisotropy factor (α_c/α_a) of Nb_3As_2C and Nb_3P_2C were lower than the ones of the corresponding 211 phases. The best isotropy performance was found in Nb_3P_2C (α_c/α_a = 1.11). Moreover, our first-principles calculations demonstrate that the weaker chemical bonding between Nb-As/P than Nb-C induces thermal expansion in M_3A_2X phases. Furthermore, a relatively weaker anharmonic effect in 321 phases than in the 211 phases was revealed by the as-calculated average Grüneisen parameters, which account for the lower TECs in 321 phases. The low TECs and enhanced thermal isotropy make 321 phases outstanding among MAX phases, which could be sound candidates for varying-temperature structural-functional components.

1. Introduction

MAX phases [1–3] are a series of layered ceramics in a general chemical formula of $M_{n+1}AX_n$, in which M = transition metals, A = main group elements, X=C/N/B, and n = 1–6. With more and more new MAX phases being discovered, including MAX borides [4–10], high/middle-entropy MAX phases [11–15], and so on, the MAX phases have been expanded to a big family with more than 160 members. Due to their layered biomimetic microstructure like abalone, superior mechanical properties were found in them [16]. Meanwhile, due to the coexistence of good performance [16,17] on thermal stability and electrical/thermal conductivity, MAX phases show promising application prospects as structural and functional materials [16,18]. Generally, the structure of MAX phases can be regarded as an alternating stacking of single MA-layer and n-layers of MX-layers [19]. The most common MAX phases are 211, 312, and 413 phases [1,2], which are named based on the number of continuously stacked MX-layers. Meanwhile, when the M site is occupied by two different metal atoms, ordering arrangement and superlattice can be found in them [20,21].

In 2019, a series of atypical MAX phases [19], named 321 phases with A = As/P, was discovered, including Nb_3As_2C, Nb_3P_2C, V_3As_2C, and Ta_3P_2C. In contrast to the single-layered MA layer in other MAX phases, the MA-triangular-prism layers of 321 phases are in a face-sharing bi-layered form. Superior elastic properties [19,22–24] of As/P-containing MAX phases were found, including large bulk modulus according to the high-pressure X-ray diffraction studies, and elastic properties based on theoretical calculations. Regarding the thermal expansion properties of As/P-containing MAX phases, only a 211 phase Nb_2AsC has been studied experimentally. The strong anisotropy (α_c/α_a = 3.66) and low thermal expansion coefficient (5.47(1) μK^{-1}) in Nb_2AsC, make it outstanding among MAX phases. While the effects of the unique MA-bilayers of As/P-containing 321 phases on their thermal expansion properties are

* Corresponding authors at: School of Materials Science and Engineering, Fujian University of Technology, Fuzhou 350118, China.
E-mail addresses: hungxchen@163.com (H. Chen), pqdai@126.com (P. Dai).

https://doi.org/10.1016/j.jmst.2023.01.022
1005-0302/

still unclear, experimental investigations are also needed to reveal their application prospects in varying temperature environments.

Here, we performed varying-temperature powder X-ray diffraction (XRD), and first-principles calculations, to reveal the influence of the introduction of MA-triangular-prism bilayers on the thermal expansion properties of 321 phases. We found the thermal expansion coefficients of 321 phases, in the range of 5-6 μK^{-1}, which are the lowest among the MAX phase family. Opposite to the larger elastic anisotropy in 321 phases, the thermal anisotropy of 321 phases is smaller than 211 phases. A typical example is Nb_3As_2C, $\alpha_c/\alpha_a = 1.44$, much lower than that of Nb_2AsC ($\alpha_c/\alpha_a = 3.66$). According to the bond distance analysis, thermal expansions of 321 phases are dominated by the dilation of the M-A (M1-A, M2-A) bonds, in which the bonding strength between M2-A is stronger than M1-A. Furthermore, based on quasi-harmonic approximation, we make further insight into the origin of the excellent thermal expansion properties of As/P-containing MAX phases. A relatively weaker anharmonic effect was found in 321 phases than in 211 phases, as indicated by the Grüneisen parameters, which should be the underlying reason for the lower thermal expansion behavior of 321 phases. Our work revealed the superior thermal expansion properties of 321 phases and the underlying mechanism behind them, experimentally and theoretically, which is helpful for their further application studies on the varying temperature uses.

2. Experimental details

Sample preparation: Samples were prepared by both the solid-state synthesis method and the molten-salt synthesis method as reported in previous works [19,25].

XRD characterizations: Low-temperature XRD patterns of Nb_3As_2C and Nb_3P_2C in the temperature range of 10–300 K were collected in a NEW Cryostat chamber (CRT-006-H5RD, Ulvac Cryogenics) with a controllable temperature range of 4 K to 300 $K \pm 0.2$ K equipped on a Rigaku SmartLab9kW with Cu K_α radiation, in which the temperature sensor is on the top of the sample. A radiation shield was equipped inside the vacuum chamber. The high-temperature powder XRD patterns of Nb_3As_2C, Nb_3P_2C, and Ta_3P_2C were collected by a Rigaku SmartLab diffractometer with Cu K_α radiation (Cu $K_{\alpha1}$: 1.5406 Å, $K_{\alpha2}$: 1.5444 Å) equipped with an Anton Paar TTK 600 chamber and a germanium monochromator in a reflection mode. A constant temperature was maintained for more than half an hour before each powder X-ray diffraction (PXRD) measurement, and a 3 °C min^{-1} heating rate was applied between the different measurements. After that, the height of the sample was adjusted for consistent alignment before each measurement. We noticed that the setting temperature may significantly differ from the actual sample temperature for high-temperature measurements. Herein, we made a temperature correction by measuring a standard silicon sample in the same measurement configuration, then taking the as-measured lattice parameters of the silicon standard sample to refer to the previously reported lattice parameter of silicon [26]. Therefore, the difference between the setting temperature and actual temperature was corrected, as shown in Fig. S1 in the Supplementary Material.

Phase/structure analysis: Multi-phase Rietveld refinements [27–29] were applied to determine the lattice parameters, atomic positions, and the phase content in the mole ratio of each as-identified phase by using the FULLPROF program suite [30].

First-principles calculations: The density functional theory (DFT) calculations were carried out by the Vienna *Ab initio* Simulation Package (VASP) [31,32] with the projector augmented wave (PAW) [33] pseudopotentials and the Perdew, Burke, and Ernzerhof (PBE) [34] for the exchange-correlation functional. The cutoff energy for the plane wave expansion was 500 eV, and the Brillouin zones were sampled by a Monkhorst and Pack [35] k-point mesh 0.02 × 2π Å^{-1} in the self-consistent calculation. The self-consistent field procedure was considered converged when the energy difference between two consecutive cycles was lower than 10^{-6} eV. Atomic positions and lattice parameters were relaxed until all the forces were less than 10^{-3} eV Å^{-1}. The Crystal Orbital Hamilton Population (COHP) analysis was carried out with the LOBSTER package [36,37]. Charge density difference was obtained by subtracting the free atomic electron densities from that of the crystals. Phonon dispersions were calculated with quasi-harmonic approximation as implemented by the Phonopy package [38]. The Grüneisen parameters $\gamma_{q\upsilon}$ for each phonon modes υ at q point was calculated by $\gamma_{q\upsilon} = -\frac{V}{\omega_{q\upsilon}}\frac{d\omega_{q\upsilon}}{dV}$. Then the average Grüneisen parameters was obtained by $(\sum_{q\upsilon}\gamma_{q\upsilon})/n_{q\upsilon}$, where $n_{q\upsilon}$ is the sum of q points and phonon modes.

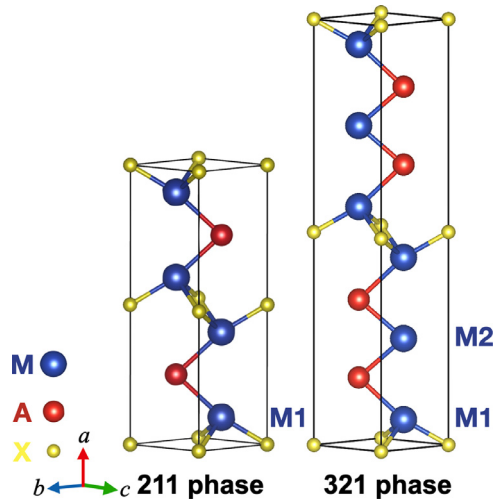

Fig. 1. The crystal structure of 211 and 321 MAX phases.

3. Results and discussion

The crystal structure of the 211 and 321 MAX phases is shown in Fig. 1. In contrast to the only one M atomic site in 211 phases, there are two kinds of M atomic sites, M1 and M2, in 321 phases with different chemical environments. M2 atoms are coordinated by six A atoms in a triangular-prism form, while one M1 atom is coordinated by three carbon atoms and three A atoms in an octahedron form.

PXRD of 321 phases at various temperatures was collected. By using the crystal structure ($P6_3/mmc$) as shown in Fig. 1, the Rietveld refinement was performed on each XRD pattern. The XRD patterns of Nb_3As_2C in selected diffraction angles at high and low temperatures, as shown in Fig. 2. A detailed room-temperature refinement results of Nb_3As_2C is given in Fig. S2, with reliability parameters $R_p = 4.50\%$, $R_{wp} = 7.08\%$. Moreover, the XRD patterns in whole measured diffraction angles are given in Figs. S3 and S4. As shown by the colored solid lines in Fig. 2, the fitted patterns are well in line with the experimental results. With the rising temperature, the peaks of (100), (105), and (110) shifted to smaller 2θ angles suggesting an increase in lattice parameters. The detailed XRD patterns and refinement results of Nb_3P_2C and Ta_3P_2C are shown in Figs. S5–S14.

Based on the Rietveld refinements, the variations of lattice parameters as a function of temperature are summarized in Fig. 3. As shown in Fig. 3(a), the lattice parameters of Nb_3As_2C obey a classical thermal expansion behavior. At low temperatures, the lattice parameters (a, c) change slightly with the temperature increase. At

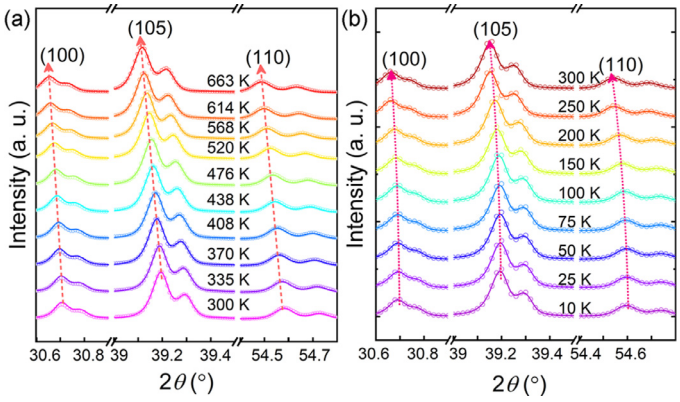

Fig. 2. Temperature-dependent XRD patterns of Nb3As2C. (a) XRD patterns collected at high temperatures (300–663 K). (b) XRD patterns collected at low temperatures (10–300 K). The colored cycles are the experimental data, and the solid lines are the calculated patterns from Rietveld refinements.

higher temperatures (200–663 K), *a* and *c* are almost linearly positively dependent on the temperature. The lattice parameters are $a = 3.35690(1)$ Å, $c = 18.6773(3)$ Å at 10 K, while they expand to $a = 3.35993(3)$ Å and $c = 18.70037(24)$ Å at room temperature and further increase to $a = 3.3653(1)$ Å, $c = 18.7432(2)$ Å at 663 K.

By using a linear fit of the temperature dependence of lattice parameters, the TECs of the as-prepared MAX phases were given by $\alpha = \frac{k}{l_0}$, in which $k = \mathrm{d}l/\mathrm{d}T$ is the slope of the as-fitted lines, l is the lattice parameter, and l_0 is the lattice parameter at 300 K. Consequently, the TEC along the *a* and *c* directions, α_a and α_c, are obtained. The average linear TEC is derived by $\alpha_L = (2\alpha_a + \alpha_c)/3$. The TECs of 321 phases and the related As/P-containing 211 phases, are determined by the same method and summarized in Table 1 alongside the reported value of Nb_2AsC [39].

Compared with the TECs of Nb_2AsC ($\alpha_a = 2.9(1)$ μK^{-1}, $\alpha_c = 10.6(1)$ μK^{-1}) [39], the value of Nb_3As_2C along the *a* direction ($\alpha_a = 4.46(4)$ μK^{-1}) is enhanced by ~54%, while the one along the *c* direction ($\alpha_c = 6.35(5)$ μK^{-1}) is significantly reduced by ~40%. Furthermore, the average linear TEC, $\alpha_L = 5.09(4)$ μK^{-1}, is ~7% smaller than the one in Nb_2AsC (5.47(1) μK^{-1}) [39], which is also the lowest among the measured MAX phases in this work. On the other hand, the thermal expansion anisotropy is valued by $\alpha_c/\alpha_a = 1.42$, much smaller than the one of Nb_2AsC ($\alpha_c/\alpha_a = 3.66$). Based on the above comparison between Nb_3AsC and Nb_2AsC, we found that Nb_3As_2C has a lower TEC and better isotropy.

In the case of Nb_3P_2C, the temperature dependence of the lattice parameter also shows a similar behavior as the one in Nb_3As_2C. Both $\alpha_a = 5.18(7)$ μK^{-1} and $\alpha_c = 5.74(7)$ μK^{-1} are lower than the ones in Nb_2PC ($\alpha_a = 5.56(8)$ μK^{-1}, $\alpha_c = 6.61(7)$ μK^{-1}). The α_L is 5.37(7) μK^{-1} which is ~9% less than the one in Nb_2PC (5.91(10) μK^{-1}). The isotropy in Nb_3P_2C ($\alpha_c/\alpha_a = 1.11$) was slightly improved compared with Nb_2PC ($\alpha_c/\alpha_a = 1.19$) but does not show such a significant difference between Nb_3As_2C and Nb_2AsC.

It should be noted that the 211 phase has never been reported in the Ta-P-C system; only the 321 phase Ta_3P_2C has been synthesized. Therefore, the comparison cannot be applied in the Ta-P-C system. The direction dependent TEC are $\alpha_a = 4.97(4)$ μK^{-1}, $\alpha_c = 5.59(5)$ μK^{-1}. The average TEC is 5.17(5) μK^{-1}. The value of $\alpha_c/\alpha_a = 1.12$ in Ta_3P_2C is close to that in Nb_3P_2C, indicating the well thermal isotropy of it.

As summarized in Table 1, the average TECs As/P-containing MAX phases are in the range of 5–6 μK^{-1}. Here we collected the reported linear TECs and the anisotropy factor of other MAX phases [39,43–57], measured by XRD or neutron diffraction. We noticed some compounds have various reported values with small/large differences, which should be caused by the different measurement conditions, including the accuracy of the as-determined temperatures and the temperature range for the linear fit. The detailed values of each phase, the linear-fit temperature range, and the characterization method are summarized in Table S2. As shown in Fig. 4, the anisotropy factors of most MAX phases are in the range of 0.5–1.5, while Nb_2AsC V_2GeC, and Nb_2SnC show abnormally strong anisotropy [39]. As shown by the red circle on the left-down corner, the TECs of As/P-containing MAX phases researched in this work are the lowest among reported MAX phases, and the anisotropy factors are close to 1.0, revealing the outstanding thermal isotropy performance of them, especially for Nb_3P_2C and Ta_3P_2C.

According to the Rietveld refinement results of single-phase Nb_3As_2C and Nb_3P_2C, the bond lengths between Nb1-C, Nb1-A,

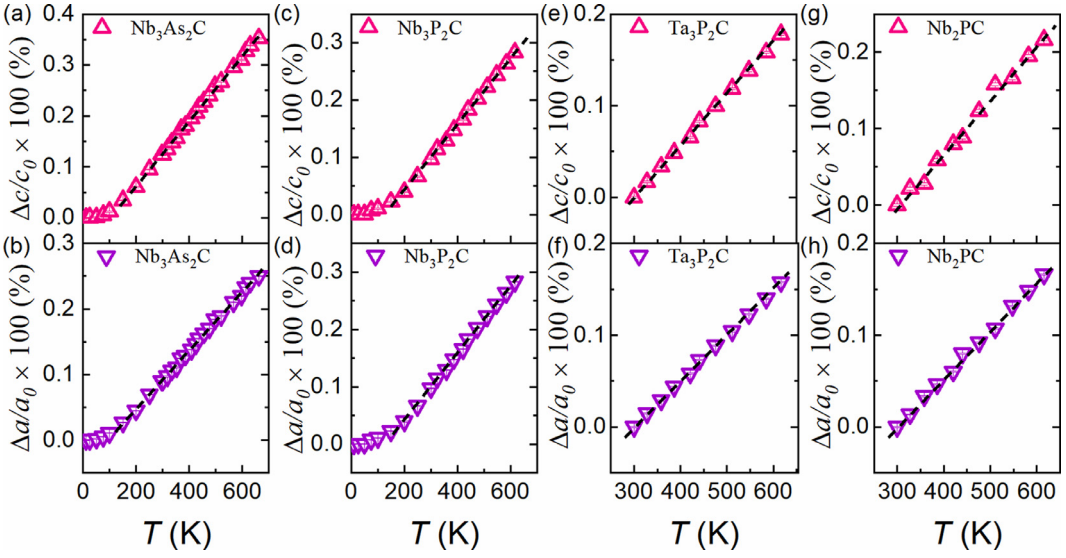

Fig. 3. Thermal expansion of 321 phases. The lattice parameter c normalized to their lowest measured value of (a) Nb3As2C, (c) Nb3P2C, (e) Ta3P2C, and (g) Nb3P2C. The lattice parameter a normalized to their lowest measured value of (b) Nb3As2C, (d) Nb3P2C, (f) Ta3P2C, and (h) Nb2PC.

Table 1
TECs derived by linear fits in the temperature range of (200–663 K), and anisotropy factor of As/P-containing MAX phases. The last column is the source of the data.

Formula	α_a (μK^{-1})	α_c (μK^{-1})	a_L (μK^{-1})	α_c/α_a	k_c/k_a	E_a/E_c	A^U	Refs.
Nb_3As_2C	4.46(4)	6.35(5)	5.09(4)	1.42	0.47	0.98	0.62	This work
					0.51	0.85	0.72	[19]
					0.60	0.95	0.55	[40]
Nb_3P_2C	5.18(7)	5.74(7)	5.37(7)	1.11	0.54	0.89	0.45	This work
					0.56	0.96	0.41	[19]
					0.54	0.94	0.43	[40]
Ta_3P_2C	4.97(4)	5.58(5)	5.17(5)	1.12	0.41	0.90	0.71	This work
					0.48	0.94	0.43	[19]
					0.52	0.95	0.42	[40]
Nb_2AsC					0.64	1.19	0.50	This work
	2.9(1) [c]	10.6(1) [c]	5.47(1) [c]	3.66[c]	0.62	1.23	0.55	[39]
Nb_2PC	5.56(8)	6.61(14)	5.91(10)	1.19	0.71	1.16	0.37	[41]
					0.65	1.07	0.35	[42]

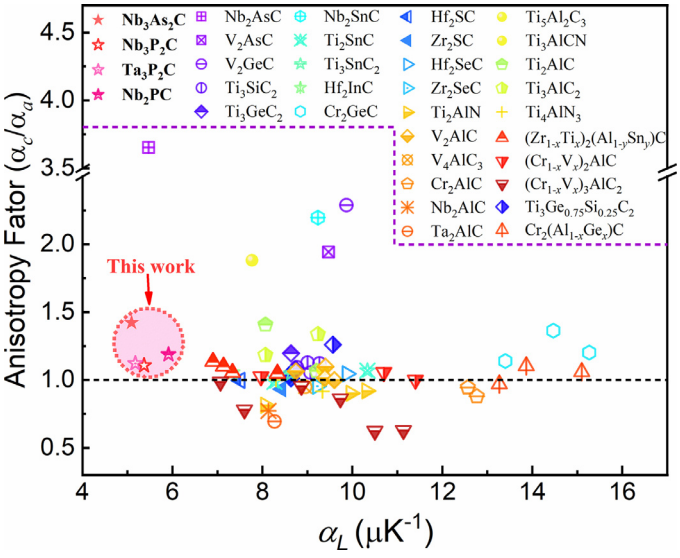

Fig. 4. The comparison of the average thermal expansion coefficient and the anisotropy factor (ac/aa) between the As/P-containing MAX phases and other MAX phases [39,43–57] obtained by diffraction methods. The red circle marks the data reported in this work. Some data are contributed by solid-solution samples, and the value x is in the range of 0–1.

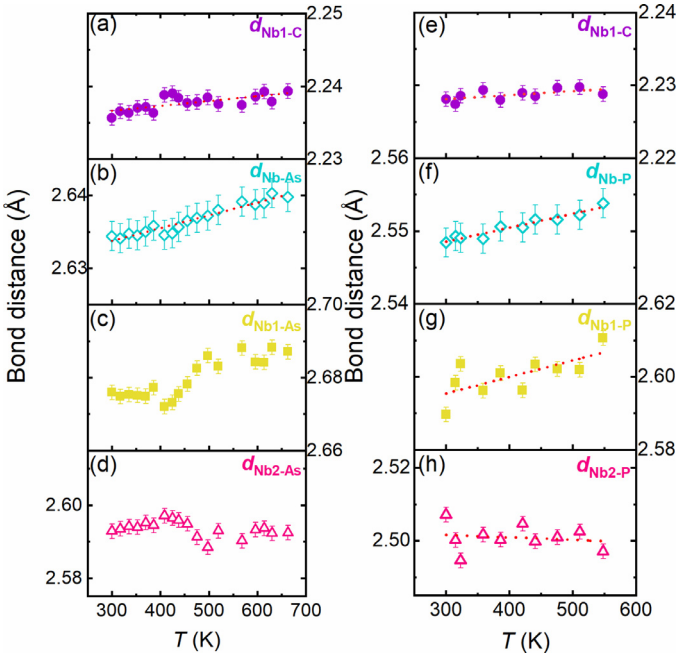

Fig. 5. Structure information of Nb3As2C and Nb3P2C obtained by single-phase Rietveld refinements. Bond lengths of (a–d) Nb3As2C and (e–h) Nb3P2C.

and Nb2-A, where A = As/P, can be obtained. As shown in Fig. 5(a), the bond length $d_{Nb1\text{-}C}$ does not change significantly with increasing temperature, ranging from 2.235 to 2.240 Å. The variations of $d_{Nb1\text{-}As}$ and $d_{Nb2\text{-}As}$ show a compensating effect, and it seems that $d_{Nb1\text{-}As}$ varied more significantly than the $d_{Nb2\text{-}As}$ bonds. While we think it should be carefully discussed because $d_{Nb1\text{-}As}$ and $d_{Nb2\text{-}As}$ are sensitive to the atomic position of A atoms. The average distance between M and A was calculated by $d_{M\text{-}A} = (d_{M1\text{-}A} + d_{M2\text{-}A})/2$. As shown in Fig. 5(b), the $d_{Nb\text{-}As}$ almost linearly increases with the rising temperature. According to the linear-fit result, the TECs of $d_{Nb\text{-}As}$ and $d_{Nb\text{-}C}$, are equal to $\alpha_{Nb\text{-}As} = 6.64(5)\ \mu K^{-1}$ and $\alpha_{Nb\text{-}C} = 3.0(8)\ \mu K^{-1}$, respectively. Similar results were found in Nb_3P_2C, in which $\alpha_{Nb\text{-}P} = 2.5(11)\ \mu K^{-1}$, $\alpha_{Nb\text{-}C} = 7.55(7)\ \mu K^{-1}$. Thereby, the bond distance of M-C did not change obviously with increasing temperature, and the thermal expansion mainly occurred in the MA layers.

Chemical bonding is essential to understand thermal expansion behavior. Thus, we performed COHP calculations to get insight into the influence of chemical bonding on the thermal expansion property. According to our calculations, the phase stability was further supported by the positive value of the partial -COHP (-pCOHP) below the Fermi level as shown in Fig. 6. The integral of the -pCOHP (ICOHP) below the Fermi surface gives the bond strength of M1-C, M1-A, and M2-A, listed in Table 2, along with the experimental and theoretical values of the bond lengths. The theoretical values of distances between neighboring atoms are slightly larger than the experimental ones, and $d_{M1\text{-}A}{}^*$ is longer than $d_{M2\text{-}A}{}^*$, consistent with the experimental results. The bond strength of M1-C, $E_{M1\text{-}C}$, in the range of 3.18–3.25 eV, is higher than those of M1-A and M2-A, indicating that M-C has a stronger covalent bonding than M-A and can resist high temperatures. Thus, the M-A bond length is sensitive to temperature, consistent with experimental observations. As shown in Table 2, the $E_{M1\text{-}C}$ of 321 phases is slightly lower than that of 211 phases. In 321 phases, the $E_{M2\text{-}A}$ is about 0.3–0.4 eV stronger than the $E_{M1\text{-}A}$. The $E_{M1\text{-}A}$ of 211 phases ranges between $E_{M1\text{-}A}$ and $E_{M2\text{-}A}$ of the corresponding 321 phases. The average bonding energy of M-A in 321 phases, $\overline{E}_{M\text{-}A} = (E_{M1-A} + E_{M2-A})/2$, is larger than that of 211 phases, with a shorter average bond distance, leading to their lower TECs.

The anisotropy of the elasticity usually can be related to the thermal expansion anisotropy [16,39,53]. Based on the elastic constants C_{ij} and compliance matrix S_{ij} derived from first-principle cal-

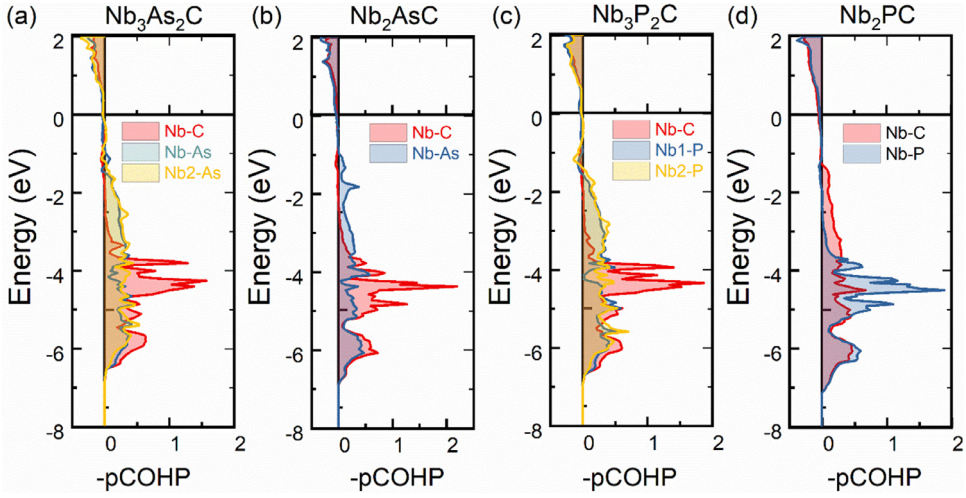

Fig. 6. The -pCOHP of (a) Nb3As2C, (b) Nb2AsC, (c) Nb3P2C, and (d) Nb2PC, where EF = 0 is the Fermi level. Positive values indicate bonding states, and negative ones are antibonding states.

Table 2
The experimental and theoretical bond distances (d), and the bonding strength (E) obtained by the integral of COHP (ICOHP) curve below the Fermi level. The theoretical bond distances by DFT are superscripted with a star symbol.

	$d_{M1\text{-}C}$ (Å)	$d_{M1\text{-}C}{}^{*}$ (Å)	$E_{M1\text{-}C}$ (eV)	$d_{M1\text{-}A}$ (Å)	$d_{M1\text{-}A}{}^{*}$ (Å)	$E_{M1\text{-}A}$ (eV)	$d_{M2\text{-}A}$ (Å)	$d_{M2\text{-}A}{}^{*}$ (Å)	$E_{M2\text{-}A}$ (eV)
Nb_3As_2C	2.2366(4)	2.2526	−3.18	2.6812(10)	2.7083	−2.31	2.5867(8)	2.6124	−2.67
Nb_2AsC	2.2292(7)	2.2416	−3.24	2.6596(10)	2.6918	−2.42			
Nb_3P_2C	2.2286(1)	2.2419	−3.22	2.594(3)	2.6154	−2.47	2.499(4)	2.5234	−2.81
Nb_2PC	2.2153(11)	2.2377	−3.25	2.5678(14)	2.5902	−2.62			

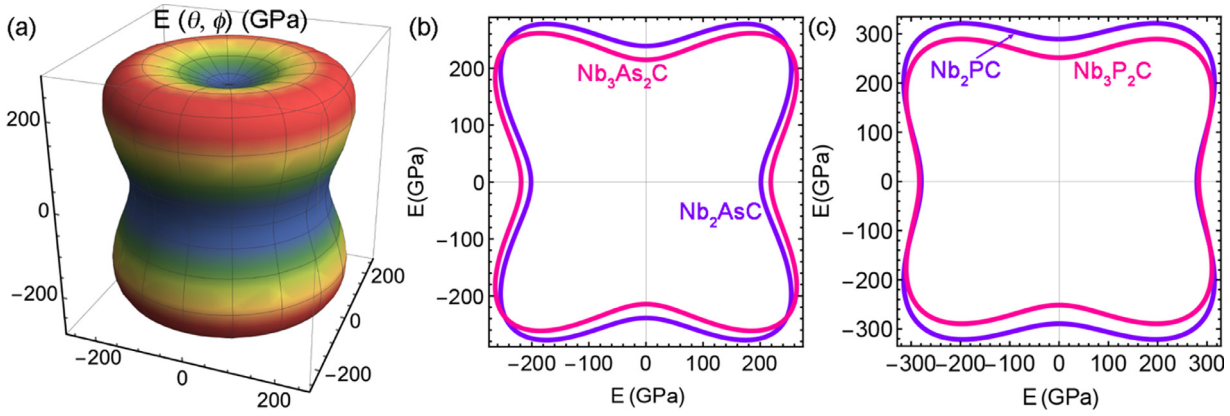

Fig. 7. Elastic anisotropy of Nb3As2C and Nb2AsC. (a) 3D plot of the direction-dependent Young's modulus of Nb3As2C. (b) Elastic anisotropy of Nb2AsC and Nb3As2C in the *xz* plane. (c) Elastic anisotropy of Nb2PC and Nb3P2C in the *xz* plane. The vertical axis and horizon axis are along the *c*-axis and *a*-axis, respectively.

culations as summarized in Table S3, the elastic modulus can be obtained. To evaluate the anisotropy, three parameters are used, including the ratio of Young's modulus along the *c* and *a* directions [58], $A_4 = E_a/E_c$, an anisotropy index for a purely dilatational deformation mode [58]

$A_5 = k_c/k_a$, and the universal elastic anisotropy index A^U [59]. The detailed equations of them are given in Supplementary Materials. The calculated values are listed in Table 1.

The departure of A_4 from 1, A_5 from 1, and A^U from zero, defines the extent of anisotropy. Based on different source data of elastic constants, the as-calculated values will show slight differences as shown in Table 1. According to our results, the A^U value of Nb_3As_2C (0.62) is larger than Nb_2AsC (0.50). Based on the A^U value and A_5 value, the elastic anisotropy is more significant in 321 phases than in 211 phases, which is contrary to the comparison of their thermal expansion properties.

The direction dependence of elastic modulus E is given here to further reveal the elastic anisotropy. For a hexagonal crystal [60], the elastic modulus can be expressed as,

$$E = 1/\left(\left(1-l_3^2\right)^2 S_{11} + l_3^4 S_{33} + l_3^2\left(1-l_3^2\right)(2S_{13}+S_{44})\right), \quad (1)$$

where $l_3 = \cos\theta$ in the polar-axis system $E(\theta,\phi)$. As shown in Fig. 7(a), the 3D view of the field-dependent Young's modulus of Nb_3As_2C is dumbbell shaped. According to the as-calculated elastic constants, a comparative plot of the directional Young's modulus in the *ac* plane of Nb_3As_2C and Nb_2AsC, Nb_3P_2C and Nb_2PC are given in Fig. 7(b, c), respectively. It should be noted that the $E_c > E_a$ in Nb_3As_2C (E_a = 214.5 GPa, E_c = 218.6 GPa) and Nb_3P_2C (E_a = 251.5 GPa, E_c = 283.2 GPa). However, in 211 phases, the E_c is smaller than E_a, Nb_2AsC (E_a = 238.8 GPa, E_c = 201.4 GPa), Nb_2PC (E_a = 298.3 GPa, E_c = 279.3 GPa). The difference in the anisotropy

of the elasticity along the *a* and *c* directions between 211 and 321 phases could be correlated to the difference in the thermal expansion anisotropy.

It is well known that thermal expansion behavior is strongly related to the anharmonic effect in lattice [61,62], which could be estimated by the Grüneisen parameter. As revealed by the calculations, the average Grüneisen parameters ($\bar{\gamma}$) of 321 phases (1.584 for Nb_3As_2C and 1.557 for Nb_3P_2C) are lower than 211 phases (1.622 for Nb_2AsC and 1.661 for Nb_2PC). This suggests the reduced anharmonic effect due to introducing more MA layers in 321 phases, which may be the underlying reason for the lower TECs in 321 phases than in 211 phases.

4. Conclusion

In this work, we give a systematical study about the thermal expansion and the elastic/thermal anisotropy of As/P-containing MAX phases, including Nb_3As_2C, Nb_3P_2C, Nb_2PC, and Ta_3P_2C, experimentally and theoretically. According to the varying temperature XRD results, their average linear TECs are in the range of 5-6 μK^{-1}, with an excellent isotropy thermal expansion behavior. Contrary to their elastic anisotropy, lower TEC and lower thermal expansion anisotropy were found in 321 phases than in 211 phases. As revealed by the COHP analysis and Rietveld refinement results, the MA layers dominate the thermal expansion behaviors, in which the bonding strength and bond distance between M2-A atoms are stronger and shorter than M1-A. Based on the quasi-harmonic approximation, the theoretical results demonstrate the smaller Grüneisen parameters in 321 phases than in 211 phases, suggesting a weaker anharmonic effect in 321 phases than in 211 phases, which should account for the lower TECs of 321 phases. The low TECs of 321 phases, which are the lowest among reported MAX phases, and the enhanced isotropy are beneficial for the future application of 321 phases in varying temperature structural-functional uses.

Declaration of Competing Interest

The authors declare that they have no known competing financial interests or personal relationships that could have appeared to influence the work reported in this paper.

CRediT authorship contribution statement

Hongxiang Chen: Conceptualization, Methodology, Investigation, Formal analysis, Writing – original draft. **Zhilong Zhang:** Software. **Jun Deng:** Conceptualization, Formal analysis, Writing – original draft. **Zhijie Lin:** Software, Investigation. **Chunfu Hong:** Methodology. **Shixuan Du:** Conceptualization, Formal analysis, Writing – original draft. **Pinqiang Dai:** Conceptualization.

Acknowledgments

This work is financially supported by the National Science Foundation for Young Scientists of China (No. 51902055), the Natural Science Foundation of Fujian Province (No. 2021J011077), and the Fuzhou Science and Technology Plan Project (No. 2021-P-049).

Supplementary materials

Supplementary material associated with this article can be found, in the online version, at doi:10.1016/j.jmst.2023.01.022.

References

[1] M. Sokol, V. Natu, S. Kota, M.W. Barsoum, Trends Chem. 1 (2019) 210–223.
[2] M.W. Barsoum, Prog. Solid State Chem. 28 (2000) 201–281.
[3] I.M. Low, Advances in Science and Technology of $M_{N+1}AX_n$ Phases, Woodhead Publishing Limited, Cambridge, 2012.
[4] Y.R. Qin, Y.C. Zhou, L.F. Fan, Q.G. Feng, S. Grasso, C.F. Hu, J. Alloy. Compd. 878 (2021) 160344.
[5] Q.Q. Zhang, Y.C. Zhou, X.Y. San, D.T. Wan, Y.W. Bao, Q.G. Feng, S. Grasso, C.F. Hu, J. Eur. Ceram. Soc. 43 (2022) 173–176.
[6] T. Rackl, D. Johrendt, Solid State Sci. 106 (2020) 106316.
[7] Y.C. Zhou, H.M. Xiang, C.F. Hu, Int. J. Appl. Ceram. Technol. 20 (2022) 803–822.
[8] T. Rackl, L. Eisenburger, R. Niklaus, D. Johrendt, Phys. Rev. Mater. 3 (2019) 054001.
[9] Q. Xu, Y.C. Zhou, H.M. Zhang, A.N. Jiang, Q.Z. Tao, J. Lu, J. Rosén, Y.H. Niu, S. Grasso, C.F. Hu, J. Adv. Ceram. 9 (2020) 481–492.
[10] Q.Q. Zhang, S. Fu, D.T. Wan, Y.W. Bao, Q.G. Feng, S. Grasso, C.F. Hu, J. Adv. Ceram. 11 (2022) 825–833.
[11] G.Q. He, Y. Zhang, P. Yao, X.C. Li, K. Ma, J. Zuo, M.S. Li, C.S. Liu, J.J. Xu, J. Mater. Sci. Technol. 137 (2023) 91–99.
[12] L.J. Qiao, J.Q. Bi, G.D. Liang, C. Liu, Z.Z. Yin, Y. Yang, H.Y. Wang, S.Y. Wang, M.M. Shang, W.L. Wang, J. Mater. Sci. Technol. 137 (2023) 112–122.
[13] S.K. Nemani, B. Zhang, B.C. Wyatt, Z.D. Hood, S. Manna, R. Khaledialidusti, W. Hong, M.G. Sternberg, S.K.R.S. Sankaranarayanan, B. Anasori, ACS Nano 15 (2021) 12815–12825.
[14] Z.G. Du, C. Wu, Y.C. Chen, Z.J. Cao, R.M. Hu, Y.Z. Zhang, J.N. Gu, Y. Cui, H. Chen, Y.Z. Shi, J.X. Shang, B. Li, S.B. Yang, Adv. Mater. 33 (2021) 2101473.
[15] Z.G. Du, C. Wu, Y.C.A. Chen, Q. Zhu, Y.L.S. Cui, H.Y. Wang, Y.Z. Zhang, X. Chen, J.X. Shang, B. Li, W.H. Chen, C.T. Liu, S.B. Yang, Adv. Energy Mater. 12 (2022) 2103228.
[16] M.W. Barsoum, M.A.X. Phases, Properties of Machinable Ternary Carbides and Nitrides, Wiley-VCH, Weinheim, 2013.
[17] X.H. Wang, Y.C. Zhou, J. Mater. Sci. Technol. 26 (2010) 385–416.
[18] Q.Y. Tan, W. Zhuang, M. Attia, R. Djugum, M.X. Zhang, J. Mater. Sci. Technol. 131 (2022) 30–47.
[19] H.X. Chen, D.L. Yang, Q.H. Zhang, S.F. Jin, L.W. Guo, J. Deng, X.D. Li, X.L. Chen, Angew. Chem. Int. Ed. 58 (2019) 4576–4580.
[20] Q. Tao, J. Lu, M. Dahlqvist, A. Mockute, S. Calder, A. Petruhins, R. Meshkian, O. Rivin, D. Potashnikov, E.N. Caspi, H. Shaked, A. Hoser, C. Opagiste, R.M. Galera, R. Salikhov, U. Wiedwald, C. Ritter, A.R. Wildes, B. Johansson, L. Hultman, M. Farle, M.W. Barsoum, J. Rosen, Chem. Mater. 31 (2019) 2476–2485.
[21] X.H. Feng, N. Li, B.Y. Chen, C. Zeng, T.Y. Bai, K. Wu, Y.H. Cheng, B. Xiao, J. Mater. Sci. Technol. 134 (2023) 81–88.
[22] M.A. Hadi, M.S. Ali, S.H. Naqib, A.K.M.A. Islam, Int. J. Comput. Mater. Sci. Eng. 02 (2013) 1350007.
[23] R.S. Kumar, S. Rekhi, A.L. Cornelius, M.W. Barsoum, Appl. Phys. Lett. 86 (2005) 111904.
[24] M.W. Barsoum, M. Radovic, Annu. Rev. Mater. Res. 41 (2011) 195–227.
[25] H.X. Chen, S. Li, J. Deng, Z.L. Zhang, J.N. Huang, F. Chang, L. Huang, S.X. Du, P.Q. Dai, J. Mater. Sci. Technol. 133 (2023) 23–31.
[26] Y. Okada, Y. Tokumaru, J. Appl. Phys. 56 (1984) 314–320.
[27] N.V.Y. Scarlett, I.C. Madsen, Powder Diffr. 21 (2006) 278–284.
[28] C. Giannini, A. Guagliardi, R. Millini, J. Appl. Crystallogr. 35 (2002) 481–490.
[29] D.L. Bish, S.A. Howard, J. Appl. Crystallogr. 21 (1988) 86–91.
[30] J. Rodríguez-Carvajal, Phys. B 192 (1993) 55–69.
[31] G. Kresse, J. Furthmüller, Comput. Mater. Sci. 6 (1996) 15–50.
[32] G. Kresse, J. Furthmüller, Phys. Rev. B 54 (1996) 11169–11186.
[33] G. Kresse, D. Joubert, Phys. Rev. B 59 (1999) 1758–1775.
[34] J.P. Perdew, K. Burke, M. Ernzerhof, Phys. Rev. Lett. 78 (1997) 1396.
[35] H.J. Monkhorst, J.D. Pack, Phys. Rev. B 13 (1976) 5188–5192.
[36] S. Maintz, V.L. Deringer, A.L. Tchougréeff, R. Dronskowski, J. Comput. Chem. 37 (2016) 1030–1035.
[37] R.Y. Rohling, I.C. Tranca, E.J.M. Hensen, E.A. Pidko, J. Phys. Chem. C 123 (2019) 2843–2854.
[38] A. Togo, I. Tanaka, Scr. Mater. 108 (2015) 1–5.
[39] T.H. Scabarozi, S. Amini, O. Leaffer, A. Ganguly, S. Gupta, W. Tambussi, S. Clipper, J.E. Spanier, M.W. Barsoum, J.D. Hettinger, S.E. Lofland, J. Appl. Phys. 105 (2009) 013543.
[40] M.A. Hadi, M.A. Rayhan, S.H. Naqib, A. Chroneos, A.K.M.A. Islam, Comput. Mater. Sci. 170 (2019) 109144.
[41] I.R. Shein, A.L. Ivanovskii, Phys. Status Solidi Basic Res. 248 (2011) 228–232.
[42] M.F. Cover, O. Warschkow, M.M.M. Bilek, D.R. McKenzie, J. Phys. Condens. Matter 21 (2009) 305403.
[43] B. Manoun, S.K. Saxena, H.P. Liermann, M.W. Barsoum, J. Am. Ceram. Soc. 88 (2005) 3489–3491.
[44] M.W. Barsoum, M. Ali, T. El-Raghy, Metall. Mater. Trans. A-Phys. Metall. Mater. Sci. 31 (2000) 1857–1865.
[45] N.J. Lane, S.C. Vogel, E.N. Caspi, M.W. Barsoum, J. Appl. Phys. 113 (2013) 183519.
[46] M.W. Barsoum, C.J. Rawn, T. El-Raghy, A.T. Procopio, W.D. Porter, H. Wang, C.R. Hubbard, J. Appl. Phys. 87 (2000) 8407–8414.
[47] S.R. Kulkarni, M. Merlini, N. Phatak, S.K. Saxena, G. Artioli, S. Gupta, M.W. Barsoum, J. Am. Ceram. Soc. 90 (2007) 3013–3016.
[48] J. Halim, P. Chartier, T. Basyuk, T. Prikhna, E.N. Caspi, M.W. Barsoum, T. Cabioc'h, J. Eur. Ceram. Soc. 37 (2017) 15–21.
[49] E.N. Caspi, P. Chartier, F. Porcher, F. Damay, T. Cabioc'h, Mater. Res. Lett. 3 (2015) 100–106.
[50] M.W. Barsoum, T. El-Raghy, C.J. Rawn, W.D. Porter, H. Wang, E.A. Payzant, C.R. Hubbard, J. Phys. Chem. Solids 60 (1999) 429–439.
[51] N.J. Lane, S.C. Vogel, M.W. Barsoum, Phys. Rev. B 82 (2010) 174109.

[52] S.R. Kulkarni, M. Merlini, N. Phatak, S.K. Saxena, G. Artioli, S. Amini, M.W. Barsoum, J. Alloy. Compd. 469 (2009) 395–400.
[53] X.D. Wang, K. Chen, E.X. Wu, Y.M. Zhang, H.M. Ding, N.X. Qiu, Y.J. Song, S.Y. Du, Z.F. Chai, Q. Huang, J. Eur. Ceram. Soc. 42 (2022) 2084–2088.
[54] T. Cabioch, P. Eklund, V. Mauchamp, M. Jaouen, M.W. Barsoum, J. Eur. Ceram. Soc. 33 (2013) 897–904.
[55] N.J. Lane, S.C. Vogel, M.W. Barsoum, J. Am. Ceram. Soc. 94 (2011) 3473–3479.
[56] G.W. Bentzel, M. Naguib, N.J. Lane, S.C. Vogel, V. Presser, S. Dubois, J. Lu, L. Hultman, M.W. Barsoum, E.N. Caspi, J. Am. Ceram. Soc. 99 (2016) 2233–2242.
[57] B. Tunca, T. Lapauw, R. Delville, D.R. Neuville, L. Hennet, D. Thiaudière, T. Ouisse, J. Hadermann, J. Vleugels, K. Lambrinou, Inorg. Chem. 58 (2019) 6669–6683.
[58] H.M. Ledbetter, J. Phys. Chem. Ref. Data 6 (1977) 1181–1203.
[59] S.I. Ranganathan, M. Ostoja-Starzewski, Phys. Rev. Lett. 101 (2008) 3–6.
[60] J.F. Nye, R.B. Lindsay, Phys. Today 10 (1957) 26.
[61] E. Grüneisen, Ann. Phys. 344 (1912) 257–306.
[62] J.S. Dugdale, D.K.C. MacDonald, Phys. Rev. 96 (1954) 57–62.